

# Phonon Trapping Lateral Field Excited Suspended Bulk Acoustic Wave Resonators (XBARS)

Elnaz Shokati, *Member, IEEE*, Robert Thomas, *Member, IEEE*, Krishna C. Balram, *Member, IEEE*

**Abstract**—Film bulk acoustic wave resonators (FBARs) underpin modern wireless communication by enabling compact, high-performance RF filters in modern smartphones. Traditionally, these FBAR devices work with quasi-plane waves of sound where the transverse extent of the acoustic field  $\gg$  the acoustic wavelength ( $\lambda_a$ ). On the other hand, strong modal confinement is needed for achieving the interaction strengths necessary for building efficient microwave to optical quantum photon transducers (MW-OT) around an FBAR opto-mechanical cavity platform. Here, we fabricate a small mode-volume phonon trapping lateral field excited FBAR resonator (XBAR) by shaping the piezoelectric layer into a spherical lens, show an improvement in modal confinement and quality factor ( $\approx 4\times$ ), and discuss the improvements needed for building efficient MW-OTs around this XBAR geometry.

**Index Terms**—FBAR, resonators, piezoelectric, MEMS, transducers, microwave to optical transducers, superconducting qubits, bulk acoustic wave

## I. INTRODUCTION

Resonant piezoelectric MEMS devices [1], [2], especially film bulk acoustic wave resonators (FBARs), underpin modern wireless communication by being the de-facto standard for implementing compact, high-performance multiband RF filters in modern smartphones [3]. Especially at high-frequencies ( $> 1$  GHz), FBARs provide the necessary combination of high electro-mechanical coupling strengths ( $k_{eff}^2$ ) and mechanical quality factor ( $Q_m$ ) that enables one to meet the stringent device requirements in terms of bandwidth, insertion loss and frequency roll-off that modern filters require, especially as we move beyond the 5G-era [4], [5]. Despite their spectacular success and continued optimization [6], one thing has remained relatively constant across the many device iterations: FBAR devices manipulate quasi-plane waves of sound [7]. The transverse extent of the acoustic field is  $\gg$  the acoustic wavelength ( $\lambda_a$ ). Historically, this is because resonator size is primarily set by impedance ( $50\ \Omega$ ) matching constraints and there has been no real device-level driver for pushing strong acoustic field confinement.

On the other hand, there are other applications where strong field confinement provides a significant advantage. The prototypical example is a piezoelectric microwave to optical quantum photon transducer (MW-OT) [8]. These devices are critical for networking remote superconducting qubit processors [9] via optical fiber networks [10] with a view towards achieving the scale necessary for achieving quantum advantage [11] on tasks such as factoring and computational chemistry. In an

Quantum Engineering Technology Labs and School of Electrical, Electronic and Mechanical Engineering, University of Bristol, Woodland Road, Bristol, UK, BS8 1UB

Email: krishna.coimbatorebalram@bristol.ac.uk

MW-OT, the microwave photon from a qubit is first converted to a mechanical mode and the optical photon conversion is mediated by an acousto-optic (AO) interaction in an optomechanical cavity [12] which supports resonant optical and mechanical modes with strong AO interaction.

To see why strong mechanical mode confinement is useful in these devices, it is helpful to consider a simplified AO interaction occurring in a 1D Fabry-Perot like cavity, where the AO interaction can be approximated [13] as:

$$g \approx \frac{\omega_c^2 n^3 p_{12}}{2c} \sqrt{\frac{\hbar}{2\rho A_{eff} L \Omega_m}} \quad (1)$$

In this expression the AO interaction strength ( $g$ ) [rad s<sup>-1</sup>] depends on a number of parameters such as the optical frequency ( $\omega_c$ ), material refractive index ( $n$ ), photoelastic coefficient ( $p_{12}$ ) mediating the interaction, density ( $\rho$ ), speed of light ( $c$ ) and Planck's constant ( $\hbar$ ) which are usually fixed once we pick a material platform of interest. The mechanical frequency ( $\Omega_m$ ) is usually set by the need to achieve phase matching (related to the Brillouin scattering frequency for bulk materials) and compatibility with current superconducting qubit operation frequencies (5-8 GHz). Given these constraints, the only way to maximize  $g$  is to reduce the cavity mode-volume ( $A_{eff} L$ ), where  $A_{eff}$  is the transverse acoustic field extent (assumed identical to the optical beam to maximize  $g$ ) and  $L$  is the cavity length. Therefore, to maximize  $g$  in the pursuit of high photon conversion efficiency ( $\propto g^2$ ), one needs strong acoustic modal confinement.

This general argument underlies why many of the state-of-the-art piezoelectric MW-OTs [14]–[16] work around small mode volume integrated photonic devices, usually 1D optomechanical crystals which support a breathing mode with strong AO interaction [17]. While they have continuously advanced in photon conversion efficiency ( $\approx 5\%$  presently) [15], they face some fundamental issues which make it worth considering alternative transducer architectures. In particular, the 1D photonic crystal geometry, and its inherent  $\lambda_a$ -scale mechanical mode confinement make it challenging to excite the mechanical mode efficiently via standard piezoelectric transducers [8]. One can circumvent this problem to an extent by using mechanical mode hybridization [18], but realizing these doubly resonant structures while preserving high  $g$  increases the fabrication complexity significantly [16]. A second issue is the large surface-to-volume ratio in these cavities which, via surface absorption, limits the optical pump power that can be used at mK temperatures, thereby putting a bound on the achievable efficiency.

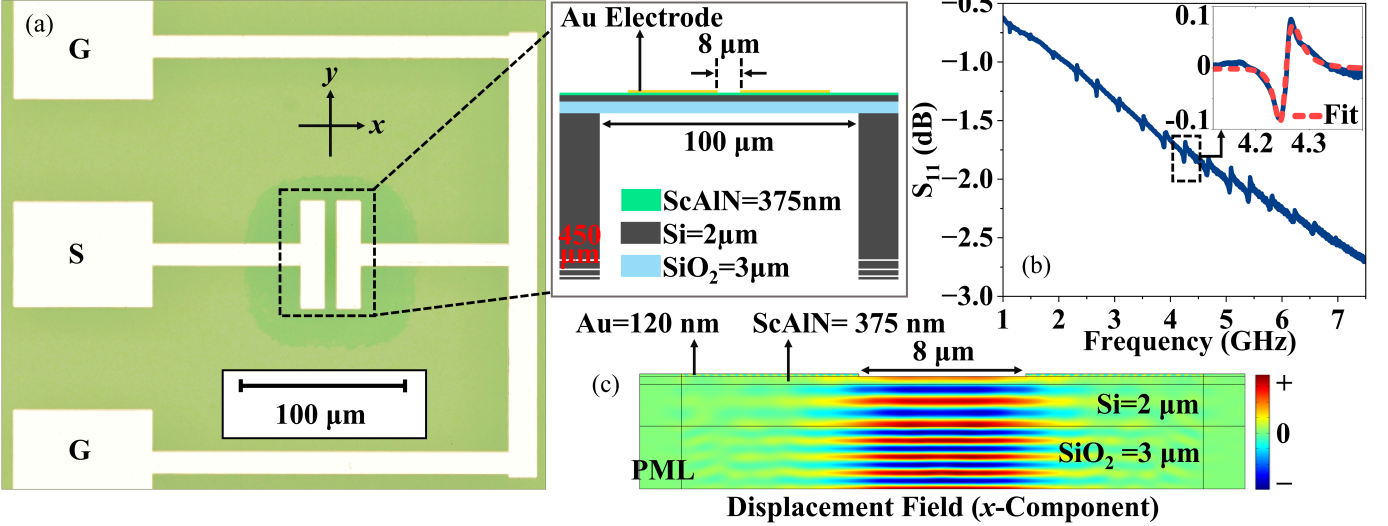


Fig. 1: (a) Microscope image of a representative XBAR device (flat-flat cavity without mode trapping) fabricated on a ScAlN-on-SOI substrate. The layer thicknesses are noted in the inset. (b) RF reflection spectrum ( $S_{11}$ ) of the device showing a series of successive overtone resonances of the cavity. A zoomed-in spectrum of one of the modes is shown in the inset showing an asymmetric (Fano) lineshape. (c) 2D FEM simulation of one of the XBAR resonances under lateral field excitation. The  $\vec{x}$ -component of the displacement is plotted clearly indicating the resonant mode has a shear horizontal (SH) character.

As an alternative architecture for building efficient MW-OT [8], high-overtone bulk acoustic wave resonator (HBAR) devices have demonstrated extremely low acoustic dissipation at cryogenic temperatures [19], [20] and can be efficiently interfaced with superconducting qubits [21] and light [22]–[24]. These elements can be combined to build a bulk MW-OT [25] around the HBAR geometry but the overall transduction efficiency is very weak ( $\approx 10^{-8}$ ). This is predominantly due to the reduction in  $g$  via the mode volume scaling argument outlined above. For reference,  $g/2\pi$  [Hz] in bulk systems is  $\approx 5$  Hz [25] whereas it is  $\approx 1$  MHz in nanobeam cavities [26]. A second issue is that the traditional FBAR / HBAR geometry [1] is not well-suited for optical interfacing because the acoustic field is confined directly under the electrode which means that an optical cavity built around this geometry [27] needs to use the metal as (at least) one of the cavity mirrors which reduces the optical quality factor and has a knock-on effect on conversion efficiency.

In this work, we take a first step towards addressing these two problems. To reduce the acoustic cavity mode volume and increase  $g$ , we extend the phonon trapping approach [19], [28] from mm scale HBAR devices to demonstrate confocal cavities in suspended μm sized FBAR devices. In addition, to facilitate efficient optical interfaces, we move away from traditional thickness field excited HBAR and FBAR modes towards lateral field actuated XBAR modes [29], [30]. In such XBAR devices, the acoustic field is trapped in between the metal electrodes and as shown below, they provide a natural route towards electric actuation of the mechanics without interfering with the optical path. We show that these two ideas can be combined to demonstrate high-frequency small mode volume acoustic cavities with reduced dissipation. We also outline potential areas for improving device performance with

a view towards building viable MW-OTs around this XBAR cavity architecture.

## II. DEVICE DESIGN AND FABRICATION

Figure 1(a) shows a microscope image of a representative XBAR resonator device fabricated on a scandium aluminum nitride (ScAlN, with 7% Sc) on silicon-on-insulator (SOI) substrate with the respective layer thicknesses indicated in the inset. The membranes are fabricated by a deep reactive ion etching (DRIE Bosch process) of the silicon handle wafer with the etch process timed to stop on the silicon oxide layer. Laser lithography is then used to pattern electrodes aligned to the membrane as shown in the figure. This standard XBAR device serves as our reference, whose performance will serve as the baseline for the confocal cavity devices discussed below.

Figure 1(b) shows the measured RF reflection ( $S_{11}$ ) spectrum of the device in (a). A series of overtone resonances corresponding to successive Fabry-Perot resonances of the acoustic cavity are clearly visible. A zoomed-in inset into one of the modes is shown in the inset clearly showing that the measured resonance lineshape is asymmetric (Fano-like). The Fano lineshape arises due to the interference of the resonance lineshape (Lorentzian) with a background pathway which we currently attribute to free-space electromagnetic radiation from the probes. Fitting this lineshape (shown by the dashed red curve) allows us to extract an effective mechanical quality factor ( $Q_m$ ) of 365. In general, we find  $Q_m$  in the range of 120–365.

Figure 1(c) shows a 2D finite element method (FEM) simulation of the device cross-section for one of the resonant modes at 4.8 GHz. As outlined above, the XBAR resonances are trapped in between the metal contacts which provide a natural route towards optical interfacing with high- $Q_o$  cavities. Fig.

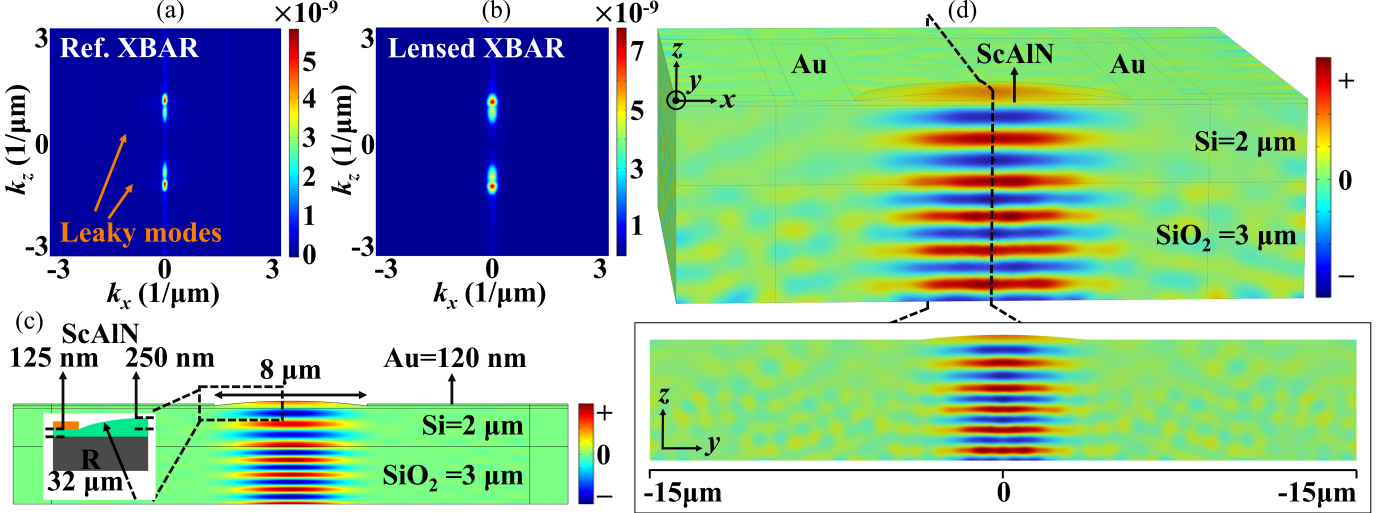


Fig. 2: Phonon trapping microcavity: By shaping the ScAlN layer into a spherical (lens-like) surface, one can prevent lateral leakage in the XBAR mode. (a) shows the  $k$ -space plot of the modal displacement of the XBAR cavity mode shown in Fig.1(c). Modes with non-zero  $k_x$  which correspond to leakage through the sides appear as circular arcs as indicated. The same  $k$ -space plot for the lensed cavity mode (c) is plotted in (b) in which the modal leakage is minimized as shown by the absence of the non-zero  $k_x$  modes. (d) 3D modal confinement is evident from a full 3D FEM simulation of the lensed cavity showing the field ( $x$  –  $z$  cross-section) is mainly confined under the lens at resonance. The inset shows the 2D cut along the orthogonal ( $y$  –  $z$ ) direction indicated by the dashed line.

1(c) also shows that the mode is a shear horizontal (SH) bulk overtone resonance with the  $\vec{x}$  component of the displacement indicated in the figure. From an MW-OT perspective, the SH mode [31] provides a key advantage over working with longitudinal modes found in HBAR / FBAR devices: the slower acoustic velocity helps reduce the Brillouin scattering frequency in silica to be compatible with the operation range of superconducting qubits (5-8 GHz) by bringing it down to 7.5 GHz from 11.5 GHz. The tradeoff with using lateral field excitation and XBAR modes is that one needs to rely on the  $e_{15}$  piezoelectric tensor coefficient of ScAlN rather than the  $e_{33}$  coefficient ( $\approx 3 \times$  larger in ScAlN). This results in a lower electromechanical coupling coefficient ( $k_{eff}^2$ ) and can be clearly seen by the size of the  $S_{11}$  resonance extinction ( $\approx 0.25$  dB). To an extent, the weaker  $k_{eff}^2$  can be compensated by higher  $Q$  as MW-OTs need operational bandwidths  $\approx 1$  MHz.

The XBAR cavity mode in this standard geometry is only weakly confined between the electrodes ( $x$ -axis) as shown by the diffraction induced mode leakage in the FEM simulation Fig.1(c). Moreover, there is no geometrical confinement along the electrode length ( $y$ -axis) which makes this geometry unsuitable for building MW-OTs on account of the reduced  $g$ . By patterning the piezoelectric layer into a curved surface [19], [28], we can spatially localize the mechanical mode and reduce the  $A_{eff}$ . In analogy with optics [32], we effectively convert a flat-flat mirror Fabry-Perot cavity which is susceptible to modal diffraction into a curved-flat cavity wherein the spherical boundary effectively serves as a spherical mirror and re-focuses the acoustic field after a cavity round-trip.

To see the effect of the lens, it is helpful to look at the modal displacement in  $k$ -space, by taking the 2D Fourier transform

of the mode displacement ( $\vec{x}$ )-component shown in Fig.1(c), shown in Fig.2(a). In an ideal scenario, we would expect four discrete peaks at finite  $\pm \beta_z$  where  $\beta_z$  corresponds to  $2\pi/\lambda_a$ , where the  $\lambda_a$  would be different in the silicon and silicon dioxide layer (ignoring the ScAlN contribution due to its thickness). As Fig.2(a) shows, we do indeed see those 4 bright spots at finite  $k_z$  and  $k_x=0$ , which are broadened to account for mode localization along  $z$ . In addition, we see faint circular arcs (indicated by orange arrows) at non-zero  $k_x$ . These correspond to lateral (leaky) bulk modes that are excited at all possible angles (hence their appearance as circular arcs in  $k$ -space).

By shaping the ScAlN layer into a spherical lens, as shown in Fig.2(c), the same mode when visualized in  $k$ -space (Fig.2(b)) shows a complete absence of the leaky modes (energy at non-zero  $k_x$ ) indicating tight confinement and higher  $Q$ . For building MW-OT, we actually need modal confinement in 3D to maximize the AO interaction. Fig.2(d) shows a 3D FEM simulation of the trapped lensed mode at resonance showing the energy is localized under the lens. We observe some excess lateral leakage in our 3D simulation compared to the 2D results and the trapped modes are not as pure as the ones we calculate via 2D FEM simulations.

The two key geometrical parameters of the lens that we can control are the radius of curvature ( $R$ ) and the lateral width ( $w$ ) which sets the size of the spherical cap and determines the overall lensing and modal confinement. The size  $w$  is mainly set by the inter-electrode gap, which is chosen as a compromise between two competing factors. Very small electrode gaps  $< 4 \mu\text{m}$  require tight focusing, high aspect ratio, small  $R$  lens shapes which are difficult to fabricate. On the other hand, larger gaps both increase mode volume

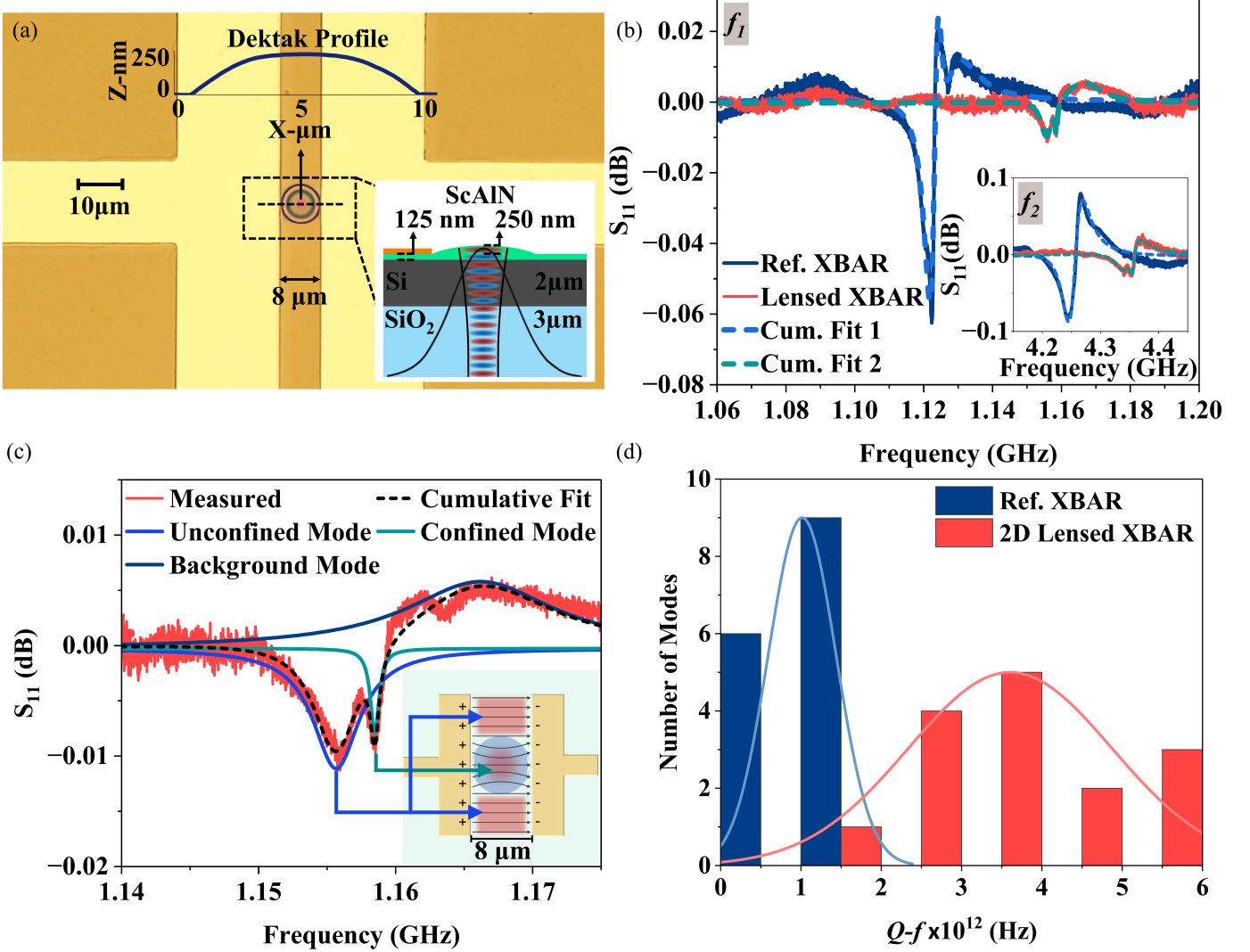


Fig. 3: (a) Microscope image of a representative lensed XBAR membrane device showing the spherical lens embedded in the ScAlN piezoelectric film. The cross-section of the device is shown in the inset with a Gaussian mode trapped in the cavity shown by illustration. The topography of the lens as measured by a profilometer (Dektak) is also shown via overlay. (b) RF reflection ( $S_{11}$ ) spectrum for a representative mode in a lensed device (red) with the same mode in a reference (unlensed) device (blue) shown for comparison ( $f_1$ ). A higher frequency comparison ( $\approx 4.3$  GHz) is shown in the inset ( $f_2$ ). The  $S_{11}$  spectra are normalized to remove the background tilt, cf. Fig.1(b). (c) Zoom-in  $S_{11}$  spectrum of the lensed device clearly showing a doublet with two modes with different  $Q$ . The lower  $Q$  mode corresponds to the untrapped mode existing in the base ScAlN layer and the higher  $Q$  mode is trapped in the lens region, as shown schematically in the inset. (d) Histogram of the measured  $fQ$  product of the modes from lensed vs reference devices showing that lensed devices give an overall  $4\times$  improvement in  $Q$ .

(lower  $g$ ) and also reduce the overall  $k_{eff}^2$  by lowering the device capacitance. Traditional XBAR devices get around this problem by using interdigitated electrodes that can help boost the capacitance, but this can not be applied directly to MW-OT because we are ultimately interested in co-localizing acoustic and optical fields. An electrode gap of  $8\text{ }\mu\text{m}$  is therefore chosen in our experiments.

$R$  for the lens is determined mainly by our ability to faithfully transfer the spherical cap pattern from the photoresist to the piezoelectric ScAlN layer. As detailed in our process flow in Appendix A, the spherical lenses are made by reflowing photoresist by baking which is known to produce a

spherically smooth surface. The actual shape of the surface ( $R$ ) can be controlled (to an extent) via the reflow temperature and time [33], and we find that the polymer surface is very close to a spherical cap in practice, as measured by a surface profilometer. This shape is then transferred to the ScAlN layer (cf. Fig.3(a)) by reactive ion etching (RIE) and the shape of the lens is modified during this process from being a spherical cap to more of a flatter top spherical frustum according to the etch selectivity. Ensuring this pattern transfer maintains exact 3D shape fidelity is challenging due to the differential etching rates of the polymer and the ScAlN (etch selectivity 1.47),

and the need to over-etch slightly to ensure the polymer is completely removed.

Figure 3(a) shows a representative fabricated phonon trapping XBART device with a spherical lens embedded into the ScAlN layer. The total ScAlN device layer thickness is  $\approx 375$  nm, the lens is designed with an  $R$  of  $32 \mu\text{m}$  and the lensed part is  $250$  nm thick. This leaves a residual  $125$  nm ScAlN base layer on which the electrodes sit as shown in the inset of Fig.3(a). The shape of the lens as measured by a profilometer (Dektak) is shown via overlay in Fig.3(a) clearly showing the flattened top after pattern transfer.

### III. CHARACTERIZATION

Figure 3(b) shows a representative RF reflection ( $S_{11}$ ) spectrum of the lensed device (in red). A similar frequency mode from a reference (unlensed) device (as in Fig.1) is also shown for reference (in blue). The  $S_{11}$  spectra are normalized to remove the background tilt (cf. Fig.1(b)). The bare device shows a larger  $S_{11}$  dip on account of the larger volume of ScAlN ( $375$  nm). More interesting is the spectrum of the lensed device (in red). Fig.3(c) shows a zoom-in to the mode which clearly shows a doublet with two modes with very different  $Q$ . The lower  $Q$  mode arises due to the unconfined mode being excited in the base ScAlN layer ( $t=125$  nm), whereas the higher  $Q$  mode is trapped in the central lens region. This is schematically illustrated in the inset of Fig.3(c). We see these higher  $Q$  modes across all frequencies, with one of the higher frequency ( $4.25$  GHz) modes shown in the inset of Fig.3(b).

We can quantify the  $Q$  improvement by plotting a histogram of the  $fQ$  product for both lensed and reference devices, wherein we take the higher  $Q$  mode to represent the trapped mode. Such a histogram is shown in Fig.3(d) which clearly shows that adding a spherical lens helps improve  $Q$  by  $\approx 4\times$ . While the  $Q$  improvement is a promising signature, it does not directly point to spatial mode confinement (phonon trapping) under the lens, which is also critical for MW-OTs. Ideally, one would like to locally map the displacement at the two frequencies (corresponding to the unconfined and lensed modes) and show that the spatial mode confinement is correlated with  $Q$ . We attempted the spatial mode mapping, but were unable to resolve the acoustic displacement in these XBART devices, due to a combination of low  $k_{eff}^2$ , and the shear mode nature which places the predominant displacement along  $\vec{x}$  instead of the out-of-plane component  $\vec{z}$ , which is what we are sensitive to. From simulation, the surface  $\vec{z}$  is lower than  $\vec{x}$  by  $\approx 40$  (2D) -  $100$  (3D)  $\times$  for these devices.

In the absence of direct mode mapping, we turn to control experiments to infer mode localization. Figure 4(a) shows a 1D variant of the lens where the mode confinement is engineered along only one axis ( $x$ ), between the electrodes. Figure 4(b) shows the  $S_{11}$  spectrum of such a 1D-lens device. We overlay the spectra of the reference (unetched) XBART device and the 2D lens device as well. We can see that the  $S_{11}$  dip of the 1D-lens device is lower than the bare device on account of reduced piezoelectric material volume. The bare device has a uniform film of  $375$  nm thickness, whereas the 1D-lens is shaped like

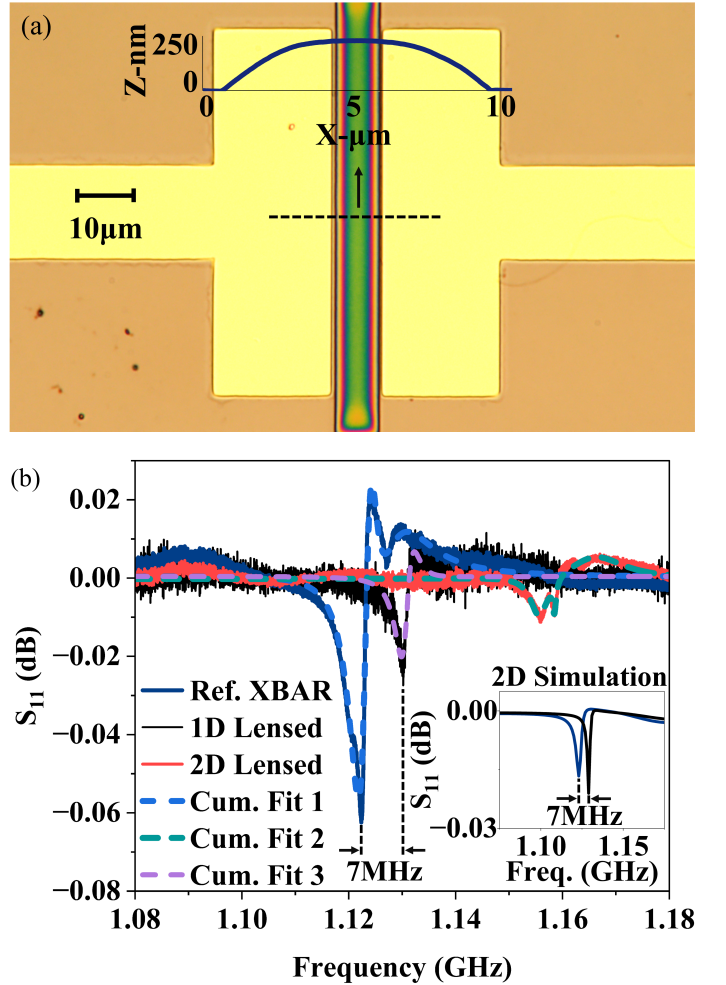


Fig. 4: Microscope image of a 1D lensed XBART device mode-trapping cavity fabricated on ScAlN using a reflow etching process, along with a Dektak scan showing a lens thickness of  $250$  nm and a radius of  $32 \mu\text{m}$ , placed between electrodes with a gap of  $8 \mu\text{m}$ . (b) RF reflection ( $S_{11}$ ) comparison between bare, 1D-lens and 2D-lens devices. The shift in frequency between the bare and the 1D lens devices agrees well with the 2D FEM simulation (inset) showing the geometry works as intended. The 2D lens data has additional structure due to the presence of the background mode (cf. Fig.3(c)).

the inset of Fig.3(a). More importantly, the frequency shift between the reference and 1D-lens device ( $7$  MHz) agrees very well with 2D FEM results (shown in the inset). This proves, at least for 1D confinement, the phonon trapping works as intended.

The 2D lens is further shifted compared to the 1D lens device and the spectrum is more complicated. This is because of the presence of the background XBART modes in the  $125$  nm ScAlN layer, as shown by the red shaded regions in the inset of Fig.3(c). Making an unambiguous frequency shift comparison with FEM, as before in the 1D lens case, is more challenging here because of numerical issues related to mesh size and the presence of additional modes in the 3D volume. Nevertheless, the frequency trend from unconfined to 1D to 2D confinement

is correct and the  $Q$  factor increases as expected, so we believe this provides evidence for acoustic mode trapping in these lensed XBAR devices.

#### IV. CONCLUSIONS

While we have shown small mode volume XBAR resonators in this work, a few issues need to be addressed before these devices can operate as efficient MW-OTs. First, the  $k_{eff}^2$  needs to be improved for efficient conversion between microwave and acoustic fields. As noted above, in comparison to traditional HBAR devices [1], XBAR devices have lower  $k_{eff}^2$  on account of both reduced device capacitance and using a weaker piezoelectric coefficient. Part of this is inevitable as separating the metals to accommodate the optical cavity necessitates relying on fringing fields. Within the constraints of the XBAR geometry as presented here, there are a few potential solutions to increase  $k_{eff}^2$  moving forward. One is to increase the Sc coefficient in the ScAlN film which automatically boosts the  $k_{eff}^2$  [34]. Secondly, one can redesign the electrodes to maximize overlap with the lens. The flat electrode geometry is not optimal for excitation of the trapped mode. Instead, semi-circular electrodes with small gaps which follow the lens shape will help improve  $k_{eff}^2$ . Finally, one can incorporate a microwave cavity to help boost the effective applied voltage  $V$ .

The second issue relates to improvement in  $Q$ . While we have clearly shown an improvement in  $Q$  over the reference XBAR mode, the highest  $Q$  we observe in our devices are  $\approx 2045$  and our  $fQ$  products overall are  $< 6 \times 10^{12}$  which is lower than both bulk HBAR and integrated phononic devices [20], [35]. In contrast to traditional HBAR and FBAR devices, as the acoustic field overlap with the metal is minimized, XBAR devices should in principle have lower acoustic dissipation. Understanding the residual sources of loss and leakage, especially from 3D FEM simulations, and working out the optimal lens shape given fabrication constraints is a key element to improving overall device performance. As noted above, since MW-OTs are expected to have operating bandwidths around 1 MHz, improvements in  $Q$  can help mitigate a lower overall  $k_{eff}^2$ .

Finally, while we have focused purely on the mechanical aspects of MW-OTs in this work and have been (mechanical) frequency agnostic in some sense, MW-OTs in this XBAR-like geometry can only achieve high  $g_0$  while operating at the Brillouin frequency [13], [27], [31]. This dictates the choice of the materials as the Brillouin frequency is set by both the material's refractive index and the speed of sound. To achieve an interaction at 7.5 GHz [31] to be compatible with current qubit frequencies, the Si layer in the current stack must be eliminated and the XBAR designed around an ScAlN-SiO<sub>2</sub> stack. Given the importance of mechanical dissipation in MW-OT [18], the  $Q$  that can be obtained in SiO<sub>2</sub> at low temperatures and GHz frequencies will be critical to achieving high conversion efficiencies. We would like to end by noting that while we have developed these phonon trapping ideas mainly in the context of of MW-OTs, they are also applicable to improving the performance (mainly  $Q$ ) of

traditional XBAR resonators and RF filters [30], where the interdigitated electrode gaps can be re-designed as 1D-lenses, similar to Fig.4.

#### V. ACKNOWLEDGEMENTS

We would like to thank Stefano Valle and Vinita Mittal for early work in this area, and Mahmut Bicer and Haoyang Li for feedback on the manuscript. This work was supported by the European Research Council (758843), the U.K.'s Engineering and Physical Sciences Research Council (EP/T517872/1, EP/N015126/1, EP/W035359/1) and the UKRI Frontier Research Guarantee (EP/Z000688/1). The ScAlN-on-SOI wafers were acquired from Tyndall Institute as part of an EU-Ascent+ program (871130, 654384), and we thank Veda Sandeep Nagaraja for guidance. ES would like to acknowledge support from the University of Bristol's EPSRC Impact Acceleration Account (IAA) .

#### APPENDIX A: DEVICE FABRICATION

Figure 5 illustrates the fabrication steps for the phonon-trapping lateral-field-excited suspended XBAR. The process uses standard MEMS fabrication techniques, including back-side patterning, substrate etching with a SiO<sub>2</sub> hard mask, and membrane release using a deep reactive ion etch (DRIE Bosch) process. As ScAlN is susceptible to standard silicon wet etchants (like potassium hydroxide (KOH) and tetramethyl ammonium hydroxide (TMAH)), during membrane release, a DRIE etch was used to etch through the silicon substrate to release the membrane.

To etch 450  $\mu$ m of silicon, a 5  $\mu$ m-thick SiO<sub>2</sub> layer was deposited on the Si substrate using plasma enhanced chemical vapor deposition (PECVD) as a hard mask. After coating the sample with photoresist, a square window for the dip etch was patterned and developed on the mask, followed by etching the SiO<sub>2</sub> window using BOE. After the Bosch silicon etch, a brief BOE etch was applied to remove a few microns of oxide on the backside of the membrane. Finally, the sample was examined and cleaned with O<sub>2</sub> plasma prior to membrane release.

Following membrane release, 1D and 2D lenses were fabricated on the 375 nm-thick ScAlN layer, with lens thicknesses of approximately 250 nm and radii ( $R$ ) of  $\approx 32$   $\mu$ m. The remaining ScAlN thickness beneath the lenses was around 125 nm, as shown in the inset of Fig.3(a).

Lens fabrication employed a photoresist reflow process: the photoresist was initially patterned into cylindrical shapes, then reflowed into hemispherical forms driven by polymer chain mobility and surface tension [33]. Once the desired lens shapes were obtained, plasma etching was used to remove the photoresist and transfer the lens pattern to the substrate, with a selectivity of approximately 1.47.

The lens radius of approximately 32  $\mu$ m is chosen based on practical considerations in transferring the reflowed photoresist pattern onto the ScAlN layer while preserving a smooth, nearly spherical surface. Control over the radius ( $R$ ) is achieved in part by adjusting the photoresist reflow temperature and duration [33]. Profilometer measurements confirm that the final lens shape closely resembles a spherical cap, with a slight

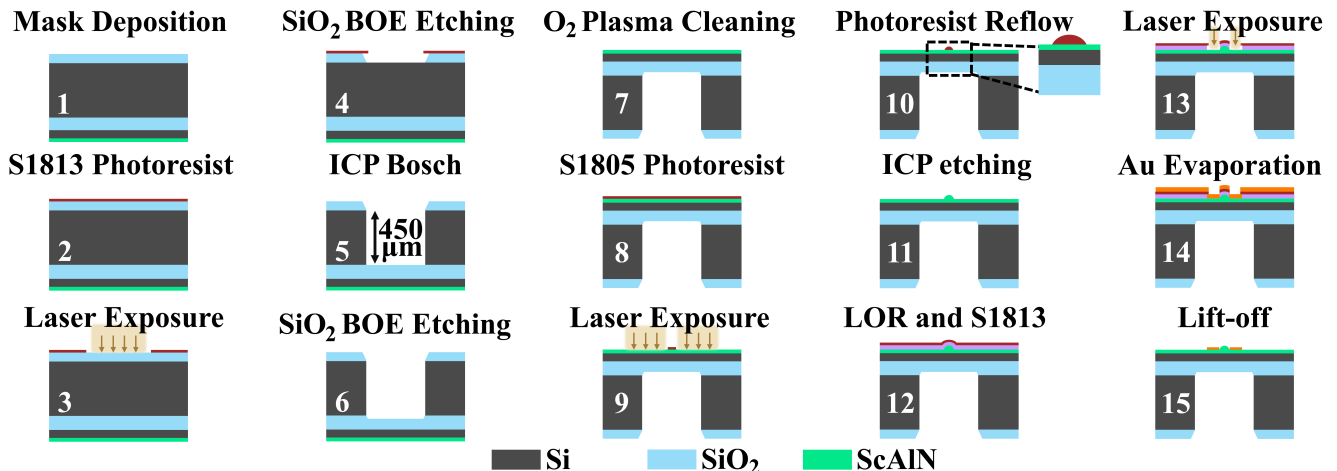


Fig. 5: Schematic illustration of the lensed XBART fabrication process. The process includes backside patterning and substrate etching using a  $\text{SiO}_2$  hard mask, membrane release via deep reactive ion etching (ICP Bosch), and subsequent lens fabrication on a 375 nm-thick ScAlN layer using photoresist reflow and plasma etching. 1D and 2D lenses are formed with final thicknesses of  $\sim 250$  nm and radii of  $\sim 32$   $\mu\text{m}$ . This is followed by standard lithography steps for electrode fabrication, including gold evaporation and lift-off. S1805 and S1813: photoresists, LOR: lift-off resist, BOE: buffered oxide etch.

flattening at the top. Finally, Cr/Au electrodes are patterned around the lens using another aligned lithography step.

## REFERENCES

[1] K.-y. Hashimoto, *RF bulk acoustic wave filters for communications*. Artech House, 2009.

[2] H. Bhugra and G. Piazza, *Piezoelectric MEMS resonators*. Springer, 2017.

[3] R. Ruby, "A snapshot in time: The future in filters for cell phones," *IEEE Microwave Magazine*, vol. 16, no. 7, pp. 46–59, 2015.

[4] S. Mahon, "The 5g effect on rf filter technologies," *IEEE Transactions on Semiconductor Manufacturing*, vol. 30, no. 4, pp. 494–499, 2017.

[5] A. Hagelauer, R. Ruby, S. Inoue, V. Plessky, K.-Y. Hashimoto, R. Nakagawa, J. Verdu, P. de Paco, A. Mortazawi, G. Piazza *et al.*, "From microwave acoustic filters to millimeter-wave operation and new applications," *IEEE Journal of Microwaves*, vol. 3, no. 1, pp. 484–508, 2022.

[6] R. Ruby, "A decade of fbar success and what is needed for another successful decade," in *2011 Symposium on Piezoelectricity, Acoustic Waves and Device Applications (SPAWDA)*. IEEE, 2011, pp. 365–369.

[7] K. C. Balram, "Piezoelectric phononic integrated circuits," *Applied Physics Letters*, vol. 125, no. 20, 2024.

[8] K. C. Balram and K. Srinivasan, "Piezoelectric optomechanical approaches for efficient quantum microwave-to-optical signal transduction: the need for co-design," *Advanced Quantum Technologies*, vol. 5, no. 3, p. 2100095, 2022.

[9] J. C. Bardin, D. Sank, O. Naaman, and E. Jeffrey, "Quantum computing: An introduction for microwave engineers," *IEEE Microwave Magazine*, vol. 21, no. 8, pp. 24–44, 2020.

[10] S. Bravyi, O. Dial, J. M. Gambetta, D. Gil, and Z. Nazario, "The future of quantum computing with superconducting qubits," *Journal of Applied Physics*, vol. 132, no. 16, 2022.

[11] T. Hoefer, T. Häner, and M. Troyer, "Disentangling hype from practicality: On realistically achieving quantum advantage," *Communications of the ACM*, vol. 66, no. 5, pp. 82–87, 2023.

[12] M. Aspelmeyer, T. J. Kippenberg, and F. Marquardt, "Cavity optomechanics," *Reviews of Modern Physics*, vol. 86, no. 4, pp. 1391–1452, 2014.

[13] W. Renninger, P. Kharel, R. Behunin, and P. Rakich, "Bulk crystalline optomechanics," *Nature Physics*, vol. 14, no. 6, pp. 601–607, 2018.

[14] M. Mirhosseini, A. Sipahigil, M. Kalaei, and O. Painter, "Superconducting qubit to optical photon transduction," *Nature*, vol. 588, no. 7839, pp. 599–603, 2020.

[15] W. Jiang, F. M. Mayor, S. Malik, R. Van Laer, T. P. McKenna, R. N. Patel, J. D. Witmer, and A. H. Safavi-Naeini, "Optically heralded microwave photon addition," *Nature Physics*, vol. 19, no. 10, pp. 1423–1428, 2023.

[16] M. J. Weaver, P. Duivestein, A. C. Bernasconi, S. Scharmer, M. Lemang, T. C. v. Thiel, F. Hijazi, B. Hensen, S. Gröblacher, and R. Stockill, "An integrated microwave-to-optics interface for scalable quantum computing," *Nature nanotechnology*, vol. 19, no. 2, pp. 166–172, 2024.

[17] J. Chan, A. H. Safavi-Naeini, J. T. Hill, S. Meenehan, and O. Painter, "Optimized optomechanical crystal cavity with acoustic radiation shield," *Applied Physics Letters*, vol. 101, no. 8, 2012.

[18] M. Wu, E. Zeuthen, K. C. Balram, and K. Srinivasan, "Microwave-to-optical transduction using a mechanical supermode for coupling piezoelectric and optomechanical resonators," *Physical review applied*, vol. 13, no. 1, p. 014027, 2020.

[19] S. Galliou, M. Goryachev, R. Bourquin, P. Abbé, J. P. Aubry, and M. E. Tobar, "Extremely low loss phonon-trapping cryogenic acoustic cavities for future physical experiments," *Scientific reports*, vol. 3, no. 1, p. 2132, 2013.

[20] V. J. Gokhale, B. P. Downey, D. S. Katzer, N. Nepal, A. C. Lang, R. M. Stroud, and D. J. Meyer, "Epitaxial bulk acoustic wave resonators as highly coherent multi-phonon sources for quantum acoustodynamics," *Nature communications*, vol. 11, no. 1, p. 2314, 2020.

[21] Y. Chu, P. Kharel, W. H. Renninger, L. D. Burkhart, L. Frunzio, P. T. Rakich, and R. J. Schoelkopf, "Quantum acoustics with superconducting qubits," *Science*, vol. 358, no. 6360, pp. 199–202, 2017.

[22] P. Kharel, G. I. Harris, E. A. Kittlaus, W. H. Renninger, N. T. Otterstrom, J. G. Harris, and P. T. Rakich, "High-frequency cavity optomechanics using bulk acoustic phonons," *Science advances*, vol. 5, no. 4, p. eaav0582, 2019.

[23] H. M. Doeleman, T. Schatteburg, R. Benevides, S. Vollenweider, D. Macri, and Y. Chu, "Brillouin optomechanics in the quantum ground state," *Physical Review Research*, vol. 5, no. 4, p. 043140, 2023.

[24] H. H. Diamandi, Y. Luo, D. Mason, T. B. Kanmaz, S. Ghosh, M. Pavlovich, T. Yoon, R. Behunin, S. Puri, J. G. Harris *et al.*, "Optomechanical control of long-lived bulk acoustic phonons in the quantum regime," *Nature Physics*, pp. 1–7, 2025.

[25] T. Yoon, D. Mason, V. Jain, Y. Chu, P. Kharel, W. H. Renninger, L. Collins, L. Frunzio, R. J. Schoelkopf, and P. T. Rakich, "Simultaneous brillouin and piezoelectric coupling to a high-frequency bulk acoustic resonator," *Optica*, vol. 10, no. 1, pp. 110–117, 2023.

[26] K. C. Balram, M. Davanço, J. Y. Lim, J. D. Song, and K. Srinivasan, "Moving boundary and photoelastic coupling in gaas optomechanical resonators," *Optica*, vol. 1, no. 6, pp. 414–420, 2014.

[27] S. Valle and K. C. Balram, "High-frequency, resonant acousto-optic modulators fabricated in a mems foundry platform," *Optics Letters*, vol. 44, no. 15, pp. 3777–3780, 2019.

[28] P. Kharel, Y. Chu, M. Power, W. H. Renninger, R. J. Schoelkopf, and P. T. Rakich, "Ultra-high-q phononic resonators on-chip at cryogenic temperatures," *Appl Photonics*, vol. 3, no. 6, 2018.

[29] J. Koulakis, J. Koskela, W. Yang, L. Myers, G. Dyer, and B. Garcia, "Xbar physics and next generation filter design," in *2021 IEEE International Ultrasonics Symposium (IUS)*. IEEE, 2021, pp. 1–5.

[30] S. Yandrapalli, S. E. K. Eroglu, V. Plessky, H. B. Atakan, and L. G. Villanueva, "Study of thin film limbo 3 laterally excited bulk acoustic resonators," *Journal of Microelectromechanical Systems*, vol. 31, no. 2, pp. 217–225, 2022.

[31] S. Valle and K. C. Balram, "Cryogenic operation of mems-based suspended high overtone bulk acoustic wave resonators for microwave to optical signal transduction," *arXiv preprint arXiv:2109.11838*, 2021.

[32] A. E. Siegman, *Lasers*. University science books, 1986.

[33] R. Kirchner and H. Schift, "Thermal reflow of polymers for innovative and smart 3d structures: A review," *Materials Science in Semiconductor Processing*, vol. 92, pp. 58–72, 2019.

[34] J. Wang, M. Park, S. Mertin, T. Pensala, F. Ayazi, and A. Ansari, "A film bulk acoustic resonator based on ferroelectric aluminum scandium nitride films," *Journal of Microelectromechanical Systems*, vol. 29, no. 5, pp. 741–747, 2020.

[35] M. Bicer and K. C. Balram, "Low-loss ghz frequency phononic integrated circuits in gallium nitride for compact radio frequency acoustic wave devices," *IEEE Transactions on Ultrasonics, Ferroelectrics, and Frequency Control*, vol. 71, no. 1, pp. 172–181, 2023.